THE JOURNAL OF PHYSICAL CHEMISTRY C

Article

pubs.acs.org/JPCC

Evidence for Ti Interstitial Induced Extended Visible Absorption and Near Infrared Photoluminescence from Undoped TiO_2 Nanoribbons: An In Situ Photoluminescence Study

Batakrushna Santara,[†] P. K. Giri,*[,†,‡] Kenji Imakita,[‡] and Minoru Fujii[‡]

[†]Department of Physics and Centre for Nanotechnology, Indian Institute of Technology Guwahati, Guwahati 781039, India

[‡]Department of Electrical and Electronic Engineering, Graduate School of Engineering, Kobe University, Kobe 657-8501, Japan

Supporting Information

ABSTRACT: Despite decades of research on the role of intrinsic defects in enhancing the performance of reduced TiO_2 based materials, unambiguous identification of defects responsible for visible light absorption, and near-infrared (NIR) photoluminescence from undoped TiO_2 has remained challenging. Herein, through in situ photoluminescence (PL) studies under a controlled environment, we investigated the origin of an extended visible absorption, visible and NIR PL emission from undoped TiO_2 nanoribbons grown by a solvothermal route. Our studies reveal that oxygen vacancies, Ti^{3+}, and F^+ center in TiO_2 are responsible for absorption in the violet and blue-green region and the PL emission in the visible region. On the other hand, absorption in the yellow-red to NIR region and PL emission in the NIR region at 1.47 and ~1.30 eV are due to Ti^{4+} and Ti^{3+} interstitials, respectively, near the surface identified for the first time. The above conclusions are supported by electron paramagnetic resonance and X-ray photoelectron spectroscopy analyses. The development of such nanoporous undoped TiO_2 nanoribbons with strong visible absorption and optical identification of Ti interstitial induced band gap states serves as an important milestone toward realizing improved visible light photocatalytic and photovoltaic applications of this novel material.

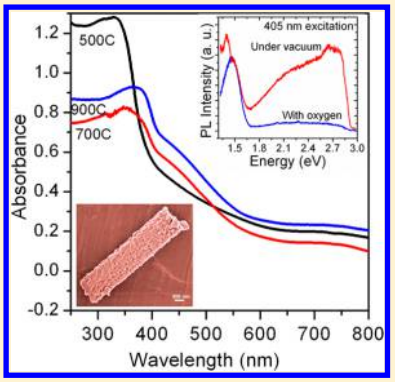

INTRODUCTION

Over the past decades, nanostructured TiO_2 is being recognized as a powerful multifunctional materials with diverse range of applications, for example, in photocatalysis,[1] photovoltaic cells,[2] humidity sensors,[3] Li ion batteries,[4] solar cells,[5] spintronic devices,[6] and so on. More importantly, defect engineered TiO_2 nanostructures have received unprecedented attention because intrinsic as well as extrinsic defects play a very crucial and fundamental role in enhancing the material/device performance. In particular, understanding the origin of red-shifts of the absorption edge of undoped reduced TiO_2 and the visible-light photoactivity of undoped and doped TiO_2 remains a hot topic of discussion.[7−10] Despite numerous studies, some of which have recognized that intrinsic defects such as oxygen vacancies (O_v) and associated defects contribute to the absorption of light in the visible spectral region,[7] a detailed understanding on the optical properties of such defects and the conditions needed for the formation of such defects remain experimentally somewhat elusive. Chen et al.[11] reported that midgap states above the valence band maximum, instead of Ti^{3+} ions associated with O_v, are responsible for the visible and infrared absorption in disordered engineered black TiO_2. Numerous theoretical as well as experimental investigations though favor the O_v model to explain the bandgap states and bandgap narrowing in TiO_2, the crucial role of Ti interstitials (Ti_i) in the near surface region for the bandgap states was elucidated by Wendt et al.[12] Earlier, through an elegant set of experiments, Henderson[13] demonstrated that the major diffusing species in the bulk-assisted reoxidation of ion-sputtered TiO_2 are Ti_i rather than O_v. However, optical spectroscopic evidence of Ti interstitials and identification of the electronic states associated with them are not established yet.

Attempts have been made to dope metal[14,15] or nonmetal[10,16] impurities to optimize the band gap of TiO_2 to visible light. However, the introduction of dopants acts as charge carrier recombination centers, which reduce the chance of the carriers to reach the particle surface to participate in the desired reaction and becomes a major issue affecting the photocatalytic efficiency.[17] Studies on the reduction of TiO_2 during the doping process have indicated the dominant role of F-type color centers in the visible-light-activity of TiO_2 photocatalysts. Recently, some approaches based on dopant-free, pure TiO_2 phase were proposed in order to overcome this limitation.[8,18] The decisive role of surface disorder and point defects, such as O_v and Ti_i in dictating the bandgap narrowing and related application of TiO_2 has been emphasized in the recent literatures. However, the actual nature of defects such as O_v and Ti_i in reduced TiO_2 and its role in the visible light photocatalysis are still under intense debate. Interestingly, both Ti_i and O_v may coexist in the reduced TiO_2 though in different

Received: August 18, 2013
Revised: September 17, 2013
Published: September 27, 2013

Table 1. Details of the Samples: Crystal Structure Obtained from XRD and Raman Studies, Morphology Obtained from FESEM and TEM Analyses, Bandgap Calculated from the Absorption Spectra, and NIR PL Peak Position in PL Spectra

						center of NIR PL peaks (eV)	
sample name	growth temperature, duration, calcinations	crystal structure	morphology	nanoribbon surface features	bandgap (eV)	peak P1	peak P2
A500	180 °C, 16 h, 500 °C	TiO_2(B)	nanoribbon	nanopits	2.34	1.21	1.47
A700	180 °C, 16 h, 700 °C	TiO_2(B)-anatase	Nanoribbon	Nanobricks	2.48		
A900	180 °C, 16 h, 900 °C	anatase-rutile	nanoribbon	smooth	2.29	1.35	1.47
A500V	A500Vac. annealed	TiO_2(B)					
B500	235 °C, 16 h, 500 °C	anatase	nanoribbon	nanopits, nanostones	2.64	1.30	1.47
B700	235 °C, 16 h, 700 °C	anatase-rutile	nanoribbon	nanostones	2.09	1.34	1.47
B900	235 °C, 16 h, 900 °C	rutile	nanoribbon	nanostones, nanobricks	1.98	1.23	1.47
C500	205 °C, 16 h, 500 °C	anatase	nanoribbon		2.77	1.27	1.47
D500	180 °C, 24 h, 500 °C	TiO_2(B)	nanoribbon	nanobricks			
D900	180 °C, 24 h, 900 °C	anatase- rutile	nanoribbon	nanostones, nanobricks	2.17		

concentration, depending on the chemical synthesis and post-growth thermal treatments under different environments. Therefore, it is important to provide a detailed description and understand the specific role of each native defect in reduced TiO_2. Native defects could influence both visible light absorption and may reduce the electron−hole recombination, which results in enhancement of highly promising photocatalytic effect in this novel material. Recently, Liu et al.[9] reported the enhanced visible light photocatalysis in Ti^{3+} self-doped TiO_2 materials. The concentration of the native defects typically depends on the growth conditions. However, the nature of bandgap states induced by the Ti_i is yet to be identified experimentally. It is therefore imperative to understand the evolution of the native defects in bandgap engineered TiO_2 nanostructures with different growth/processing conditions and identify the defects responsible for enhanced photocatalytic and photovoltaic performance.

The recent growth in theoretical interest in the electronic structure of point defects in TiO_2 has yielded powerful calculation approaches that predict more precise energy levels in the bandgap caused by O_v and Ti_i.[19,20] Though there have been some experimental confirmations of these native defects by various groups,[8,12,18,21] experimental confirmation of predicted energy levels of Ti_i have remained challenging. The diffusion of Ti_i defects from surface to bulk during heating in reduced atmosphere and opposite effect that occurs in oxygen atmosphere have been addressed by some groups.[12,13] However, the assignment of the point defects to specific photoluminescence (PL) emission in TiO_2 polymorphs (mainly anatase and rutile) remains unclear and is highly debated. Though visible PL emission is common in defective TiO_2, which has been attributed to oxygen vacancies,[22−24] there is no systematic understanding on the near-infrared (NIR) PL emission in rutile TiO_2. Some reports suggested that it is the intrinsic defects in rutile TiO_2[22,25] that gives rise to NIR PL. Montoncello et al.[26] reported the NIR PL at 1.51 eV for both phases (anatase and rutile) at low temperature (11 K), and the spectra were interpreted as the phonon replica effect, originating from ionization of oxygen vacancies. A recent report on the NIR PL emission from large bandgap ZnO was explained on the basis of donor−acceptor transition between O_v and Zn vacancies and the radiative recombination of shallowly trapped electrons with deeply trapped holes at interstitial O_i.[27] However, there is no in situ study, to the best of our knowledge, on the evolution and origin of NIR PL emission and its relation, if any, to the enhanced visible absorption in TiO_2 nanostructures in pure TiO_2(B), anatase, rutile, and its mixed phases.

Herein, through careful in situ photoluminescence studies under controlled environment, we attempt to identify the specific defect responsible for the red shift in the absorption edge, visible and NIR PL emission in undoped TiO_2 nanoribbons (NRb) grown by a solvothermal technique. In particular, monitoring the time evolution of the visible and NIR PL emissions at low temperature, under high vacuum and oxygen environment, allows us to distinguish and unambiguously identify the defect states associated with O_v and Ti_i. Interestingly, we observed a wide range of visible absorption from these undoped TiO_2 NRb fabricated under various growth conditions, and we demonstrate that Ti_i rich samples have higher red shifts in the absorption edge, which is crucial for more efficient visible light photocatalysis in TiO_2-based materials. Based on our experimental observations, the origin of the tunable NIR PL from TiO_2 NRb has been traced to surface Ti interstitials for the first time. The identification of Ti_i states in the bandgap of undoped TiO_2 NRb is considered an important step in further exploitation of defect engineered undoped TiO_2 nanostructures and is believed to be an important milestone in realizing improved visible light photocatalytic and photovoltaic applications of this novel material.

EXPERIMENTAL SECTION

The details of the synthesis procedure for the TiO_2 nanostructures were reported in our previous study.[24] Briefly, 0.275 g of anatase TiO_2 powder was mixed with 60 mL of 10 M NaOH in mixed solvent (DI water/ethylene glycol = 1:1) under stirring for 1 h, a milky solution was obtained. Afterward, the mixed solution was transferred into a Teflon-lined autoclave (Berghof, BR- 100). During the growth process, the temperature inside the autoclave was monitored and maintained at 180, 205, and 235 °C under autogenous pressure and constant magnetic stirring at 250 rpm for 16−24 h. The formed precipitates were obtained by centrifugation and washed several times with DI water. Subsequently, the products underwent an ultrasonic treatment with 0.1 M HCl until the pH ∼ 7 and finally the precipitates were calcined at different temperatures in the range 500−900 °C for 5 h in air. The vacuum annealing of the sample grown for 16 h followed by 500 °C calcinations was performed at 300 °C under 1.2×10^{-2} mbar pressure for 2 h. For convenience of discussion, the TiO_2 nanoribbon samples are categorized according to different growth temperature,

dx.doi.org/10.1021/jp408249q | J. Phys. Chem. C 2013, 117, 23402−23411

reaction duration and calcinations temperatures. Samples grown at fixed reaction temperature of 180 °C, 16 h, are categorized as "A" series and after calcination at 500, 700, and 900 °C are named as A500, A700, and A900, respectively. The A500 after vacuum annealing is named as A500V. The samples grown at 235 °C, 16 h reaction, are termed as 'B' series and after calcinations at 500, 700, and 900 °C are named as B500, B700, B900, respectively. Sample grown at 205 °C for 16 h reaction and calcined at 500 °C is named as C500. Samples grown at 180 °C after reaction time 24 h followed by calcinations at 500 and 900 °C are termed as D500 and D900, respectively. The details of the sample nomenclature and growth conditions are presented in Table 1. The characterization tools used to study various properties of the as-grown NRb are described in the Supporting Information.

RESULTS AND DISCUSSION

Structural Characterization. The XRD patterns of solvothermal products synthesized at two different growth temperatures (i.e., 180 and 235 °C) after a 16 h reaction and different calcinations temperatures are shown in Figure S1 (Supporting Information). All the peaks correspond to TiO_2(B) phase for A500; however, for A700 and A900, mixed phase TiO_2(B)-anatase and anatase-rutile TiO_2 with little signature of TiO_2(B) are observed, respectively (Figure S1a). We observed pure anatase phase for B500, mixed phase anatase-rutile for B700, and pure rutile TiO_2 for B900. At low growth (180 °C) and calcinations temperature (500 °C), pure TiO_2(B) phase is formed irrespective of reaction duration (see Figure S1c). On the other hand, at higher growth temperature of 235 °C, anatase, mixed anatase-rutile, and pure rutile phases were formed after 500, 700, and 900 °C calcinations, respectively (Figure S1b). Various phases of the as-prepared NRb were further confirmed from micro Raman analysis. Raman modes in A500, A500V, and D500 correspond to pure TiO_2(B) phase, as shown in Figure S2a (Supporting Information). The intensity of A_g mode at 147 cm^{-1} is decreased considerably for the A500V and D500 compared to A500. Because A500V is vacuum annealed, the reduction in intensity of the A_g mode is attributed to the higher concentration of oxygen vacancies. A900 and D900 show (Figure S2b) the Raman modes of mixed phase anatase-rutile, while A700 shows mixed phase TiO_2(B)-anatase, consistent with the XRD analysis. An upshift of $E_g(1)$ mode for the as-synthesized NRb compared to the precursor TiO_2 powder is shown in the inset of Figure S2b (Supporting Information). Note that the Raman mode of precursor TiO_2 powder is at 142 cm^{-1} (Figure S3, Supporting Information). The blue shift of as-synthesized NRb is primarily due to the oxygen vacancies in TiO_2.[28−30] B500 and C500 show the characteristic Raman modes of anatase TiO_2, while B900 shows the Raman modes of rutile TiO_2 (see Figure S2c, Supporting Information). B700 shows a mixed phase anatase-rutile TiO_2. The inset of Figure S2c, left panel, shows the blue shifting of the $E_g(1)$ Raman mode of the as-grown samples compared to precursor TiO_2. Note that the larger blue shift is observed for the B500 and B700 compared to C500. From the PL study discussed later, we found that C500 contains a high concentration of oxygen vacancies as compared to B500 and B700. Hence, it is likely that the blue shift of the $E_g(1)$ mode in anatase TiO_2 is not only associated with O_v, but also related to other defects, for example, Ti_i in the NRb. The Raman spectra are fully consistent with the XRD pattern for phase confirmation among different TiO_2 polymorphs.

Morphological Studies. The morphologies of the as-synthesized nanostructures imaged by field emission scanning electron microscopy (FESEM) are shown in Figure 1a (samples

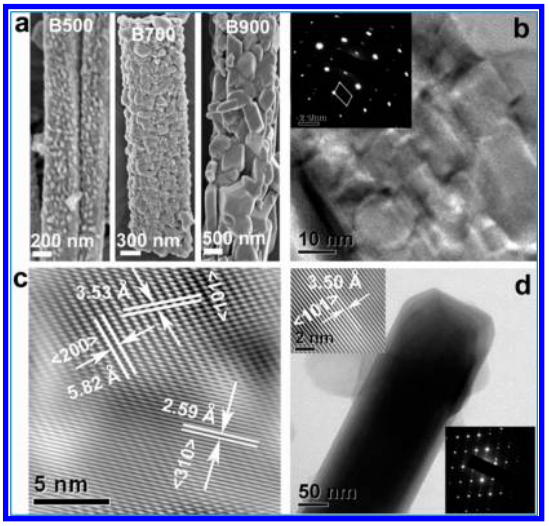

Figure 1. FESEM images of the morphology of TiO_2 nanostructures: (a) B500, B700, and B900 grown at 235 °C; TEM images of (b) A700 at higher magnification showing nanobricks and nanopits, and the inset shows the corresponding SAED pattern; (c) A700, lattice fringe; and (d) D900, the insets show the lattice fringe and SAED pattern.

B500, B700, and B900). Nanostones and nanopits, like structures on the surface of NRb, are clearly seen for B500. The growth of the nanostones on the surface of NRb is increased as the calcinations temperature is increased to 700 °C (B700). Further increase of calcination temperature to 900 °C leads to large size naobricks and nanostones like structures on the surface. These structures have sharp edges and high surface area, which may help for the enhanced photocatalytic activity at the surface. The nanostones and nanobricks are arranged in a nice pattern that builds a microbridge like structures. The NRb with moderate to high O_v and diffusion of Ti_i exhibits a wide variety of restructuring surface morphologies which includes nanopits and nanostones during various calcinations temperatures. These surface structures result from various $Ti_{lattice}$−O and Ti_i−O bond rearrangement due to the Ti interstitials that diffuse from the bulk to the surface during calcinations. Thus, the diffusion of Ti_i in TiO_2 plays a major role in surface and interface-related phenomena when high temperature calcinations are involved. This may be similar to the TiO_x (where x = ~2) islands found by Wendt et al.[12] due to the diffusion of Ti_i in their STM images during annealing. The low magnification FESEM images of A500, A700, and D500 are shown in Figure S4 (Supporting Information), which indicate complete formation of nanoribbons. The energy dispersive X-ray (EDX) spectrum of A900 is shown in Figure S5 (Supporting Information), which shows only Ti and O elements, indicating there is no impurity element. The atomic ratio of O/Ti is 1.72, which is less than 2, indicating oxygen deficiency, and thus, oxygen vacancies are present.

Figure 1b−d shows the transmission electron microscopy (TEM) images of the as-grown samples A700 and D900. The high magnification TEM image of A700 is shown in Figure 1b. Nanoribbons with nanobrick- and nanopit-like structures on

dx.doi.org/10.1021/jp408249q | J. Phys. Chem. C 2013, 117, 23402−23411

the surface are observed. The inset of Figure 1b shows the corresponding SAED pattern. It clearly dictates the tetragonal pattern of anatase TiO_2 and monoclinic pattern of TiO_2(B) phase, indicating mixed phase TiO_2(B)-anatase is formed. The nanopits of diameter 5−13 nm and nanobricks of width ∼13 nm are formed on the surface of NRb, making them porous-like structures with a highly active surface. The HRTEM lattice fringe of A700 with *d*-spacing of 5.82 and 2.59 Å corresponds to (200) and (310) planes of TiO_2(B) phase, respectively, as shown in Figure 1c. This indicates that the NRb are grown along the ⟨200⟩ direction, whereas the nanobricks are grown along the ⟨310⟩ direction. The *d*-spacing of 3.53 Å corresponds to (101) plane of anatase TiO_2. Figure 1d shows the TEM image of D900. The corresponding SAED pattern shown in the inset dictates the single crystalline nature. The HRTEM lattice image of the corresponding NRb is shown in the inset of Figure 1d, left upper panel. The lattice fringe with *d*-spacing of 3.50 Å corresponds to the (101) plane of anatase TiO_2. Thus, growth temperature, reaction duration, and calcination temperature strongly influence the surface morphology and resulting defects, for example, O_v, Ti_i, and so on, in TiO_2, and this is crucial in tuning the electrical and optical properties of the nanostructures.

Optical Absorption and Photoluminescence Studies. Light absorption characteristics of the solvothermally synthesized TiO_2 nanostructures are shown in Figure 2a,b. All the as-

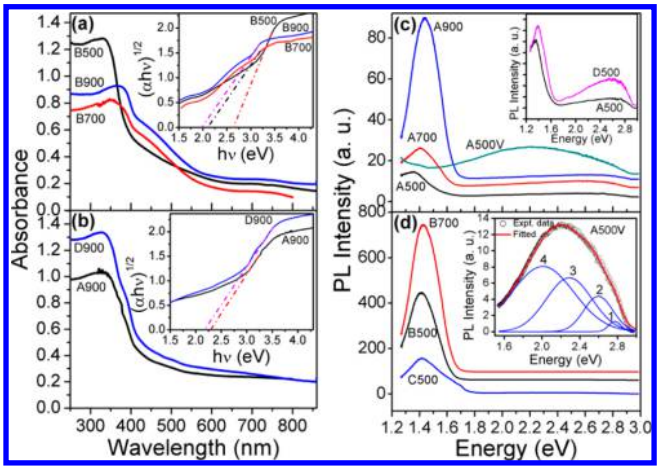

Figure 2. UV-vis-NIR absorption spectra: (a) B500, B700, and B900 grown at 235 °C and different calcinations; (b) A900 and D900 grown at different reaction duration and 900 °C calcinations; The insets in each case show the $(\alpha h\nu)^{1/2}$ vs $h\nu$ plot, indicating the indirect bandgap for the corresponding absorption spectrum of each sample. Bandgap energy is calculated from the extrapolated line (dashed) fitted to respective linear portions. Room temperature PL spectra for (c) A500, A700, A900, and A500V, inset is the comparison of A500 and D500; Spectrum for A500V is vertically shifted for clarity. (d) B500, B700, and C500, inset shows the magnified view of the visible PL in A500V with Gaussian peak fitting.

synthesized samples exhibit a red shift of the absorption edge and considerable absorption in the visible region (>447 nm) compared to precursor TiO_2 (380 nm, Figure S6, Supporting Information). The absorption spectra for B500, B700, and B900 are shown in Figure 2a. Note that with higher calcinations temperature, the absorption edge extends up to yellow region of the visible spectrum. Due to indirect bandgap, the band tail is extended to a low energy region. In Figure 2a, three steps of absorptions (i.e., 380−420, 420−580, and 660−840 nm) can be distinguished. The absorption in the 380−420 nm range (violet region) arises due to the self-trapped states and shallow trap states $Ti^{3+}_{lattice}$ centers, while absorption in the range 420−580 nm (blue, green, and yellow region) arises due to the deep trap states F^+ centers associated with the oxygen vacancies. However, the absorption in the range 660−840 nm (red region and extended up to NIR region) is prominent for samples calcined at higher temperature and it may be originated from the Ti_i defects that migrate to the near surface region during calcination. Note that B500, B700, and B900 grown at higher reaction temperature show systematic red shift in the bandgap to pure visible region, enabling strong visible absorption in the undoped TiO_2 and this is expected to exhibit strong visible light photocatalytic activity for hydrogen generation. The presence of regular lattice $Ti^{3+}_{lattice}$ trap center, F^+ center, and interstitial Ti^{3+}_i are confirmed from our electron spin resonance (ESR) measurement discussed later. Figure 2b shows the absorption spectra of the samples grown after different reaction durations (i.e., 16 and 24 h) and calcined at 900 °C. With an increase in reaction duration, visible absorption is clearly increased and this is caused by higher concentration of defects. The Tauc plot constructed from the absorption spectra are shown as insets in each case. The band gap is calculated from the linear fit to the linear portion of $(\alpha h\nu)^{1/2}$ versus $h\nu$ plot and the data are presented in Table 1. Note that the band gap of pure anatase phase of TiO_2 NRb (C500 and B500) are relatively large (2.77 and 2.64 eV, respectively) compared to the other as-grown samples. However, we noticed that within the same phase, the band gap of B500 is narrower than that of C500 grown at lower temperature. This indicates that samples grown at higher temperature followed by calcination at high temperature possess higher concentration of a particular defect that is largely responsible for reduction in the bandgap. This is consistent with the theoretical predictions made by various groups.[19,20,31] Interestingly, experimental evidence of bandgap narrowing due to Ti_i defects is reported by Wendt et al.[12] Morgan et al.[31] reported the larger red-shift of absorption edge due to Ti_i defects compared to O_v defects.

Theoretical calculations suggested that a high vacancy concentration could induce a band of electronic states just below the conduction band.[32] Zuo et al.[33] reported that the presence of a mini band closely below the conduction band minimum, which is related to the oxygen vacancy associated with Ti^{3+} and is responsible for the bandgap narrowing in TiO_2. Similar observation related to oxygen vacancy induced bandgap narrowing has been reported in ZnO system.[34] More recently, Liu et al.[9] reported the band gap narrowing of undoped TiO_2 due to oxygen vacancies and Ti^{3+} species which showed enhanced visible light-driven photocatalytic oxidation on methylene blue and water splitting. Finazzi et al.[20] reported that the presence of both $Ti^{3+}_{lattice}$ and Ti^{3+}_i species resulted in new states in the band gap (about 1−1.5 eV below the conduction band) of TiO_2 materials. It will be evident that our results are more consistent with the Ti interstitial mediated redshift of the bandgap to visible region. Note that the absorption edge of precursor TiO_2 powder is at ∼380 nm (3.26 eV), although PL studies show high concentration of oxygen vacancies present in it. Thus, oxygen vacancies alone do not give rise to visible absorption. On the other hand, high temperature calcined NRb shows considerable decrease in bandgap from 2.77 to 1.98 eV (shown in Table 1) under different growth conditions as compared to precursor TiO_2

dx.doi.org/10.1021/jp408249q | J. Phys. Chem. C 2013, 117, 23402−23411

powder (3.2 eV). Our PL data presented later is consistent with the fact that these samples contain very low vacancy concentration. Thus, the control of Ti interstitials in TiO_2 nanostructures hold the key to enhanced visible absorption and enhanced photocatalytic performance without introducing any external doping/impurities.

To enable a more clear understanding on the nature of defects and related trap states within the bandgap in TiO_2 NRb, PL studies are performed on different samples. Figure 2c shows the room temperature and atmospheric pressure PL spectra of the samples grown at 180 °C, 16 h. The vacuum annealed sample A500V shows highly enhanced visible PL emission as compared to as-synthesized A500, indicating that the concentration of oxygen vacancies are dramatically increased after vacuum annealing, as expected. However, as calcination temperature is increased from 500 to 900 °C, the intensity of NIR PL is clearly increased and the peak is blue-shifted. Similar features are observed for the samples grown at 235 °C (Figure 2d), where the PL intensity is about 1 order of magnitude higher. On the other hand, the intensity of visible PL is very low and does not change significantly with calcination temperatures. Further, comparison of PL intensity for B500 and C500 shows that NIR PL intensity is higher for growth at higher temperature (Figure 2d). Thus, it is evident that higher the growth temperature and/or higher the calcinations temperature, higher the NIR PL intensity. Further, no correlation is found between the visible PL and NIR PL intensity in each sample, which indicates that the origin of these PL emissions is associated with distinctly different defects species (i.e., O_v and Ti_i). The inset in Figure 2c shows the comparison of PL spectra for A500 and D500 that are grown/calcined at low temperature. It is clear that at low growth temperature, NIR PL intensity is very low compared to higher growth temperature and both NIR and visible PL intensity increase with reaction durations. The broad visible PL could be fitted properly with four Gaussian bands centered at 2.01, 2.29, 2.60, and 2.77 eV for A500V (inset of Figure 2d). Note that the higher energy tail of the PL spectra is truncated due to the use of a 435 nm filter during the PL measurement. Peak 1 is ascribed to self-trapped excitons located at TiO_6 octahedra, while peaks 2 and 3 are ascribed to oxygen vacancy related trap states. The peak 4 is attributed to the presence of hydroxyl (OH) species which may form an acceptor level just above the valence band.[24] Moreover, upon the loss of an O atom in TiO_2 lattice, the electron pair that remains trapped in the vacancy cavity leave behind a pair of electrons, which give rise to an F center and one of the electron in the F center tends to occupy the neighboring Ti^{4+} ion and yield $Ti^{3+}_{lattice}$ center and F^+ center states within the bandgap of the material, as detailed in ref 24. Here, we focus our attention to understand the evolution of NIR PL emission and its origin.

XPS and ESR Studies. A more direct evidence of oxygen vacancies and Ti interstitials in TiO_2 NRb, which are believed to be responsible for the visible and NIR PL emission, are further confirmed from X-ray photoelectron spectroscopy (XPS) analysis. Note that identification of Ti interstitials through XPS has been very challenging experimentally. A comparison of the Ti 2p core-level spectra for A900, A500V, and B500 is shown in Figure 3a. Interestingly, the Ti 2p3/2 and 2p1/2 peaks shows slightly lower binding energy in Ti interstitial rich A900 and B500 as compared to the case of vacancy rich A500V. Though the shift is rather small, it is discernible in the spectra and is meaningful to distinguish two

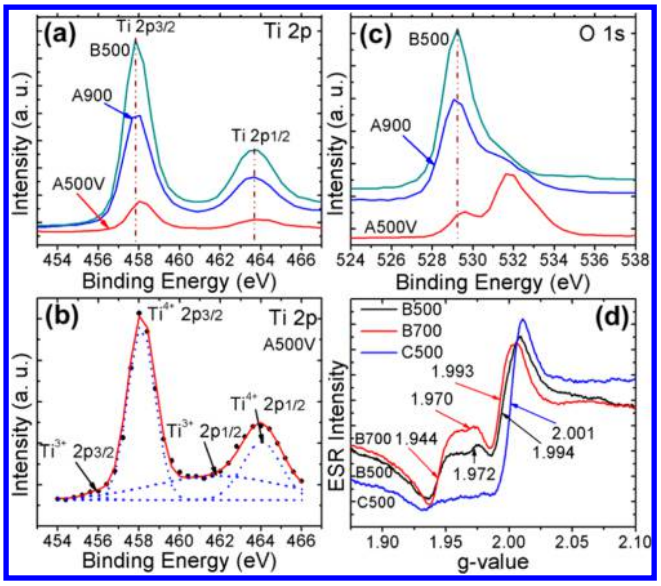

Figure 3. XPS spectra: (a) Ti 2p core level spectra for A900, A500V, and B500. Dotted vertical lines show the change in relative peak position in each case. (b) Ti 2p core level spectral fitting for A500V. Dotted curves refer to the fitting of the various components in the XPS spectrum. (c) O 1s core level spectra for A900, A500V, and B500. Dotted vertical line shows the change in relative peak position. (d) Room temperature ESR spectra for B500, B700, and C500. The respective *g*-values are indicated in each case.

different kinds of samples exhibiting different PL emissions. Note that the separation between Ti 2p3/2 and 2p1/2 peaks (5.75 eV) remains unchanged for all samples. It can be noted that no obvious broadening and shouldering of Ti 2p3/2 peaks toward lower binding energy are observed for A900 and B500, which indicates the absence of Ti^{3+} species on the surface of the NRb. Etacheri et al.[35] reported that Ti 2p3/2 peak of XPS spectra are shifted to higher binding energy in their oxygen rich TiO_2 samples due to oxygen interstitials. Therefore, the peak shift for A900 and B500 toward lower binding energy can be interpreted as a combined effect of surface Ti^{4+} and near surface Ti^{3+}_i interstitial defects. We also observed Ti^{3+}_i defects from these samples in the ESR spectra, presented later. We believe that during high temperature calcinations, the Ti^{3+}_i defects on the surface tend to interact with atmospheric O_2 in air and oxidize to form Ti^{4+}_i species. Interestingly, the deconvolution of Ti 2p core-level spectra of oxygen vacancy rich A500V yields two major characteristics doublets for Ti 2p3/2 and 2p1/2, encompassing a set of two 2p3/2 peaks at 455.85 and 458.12 eV and a set of two 2p1/2 peaks centered at 461.89 and 464.03 eV, respectively (see Figure 3b). The XPS peaks at 458.15 and 464.03 eV are attributed 4+ valence state of Ti 2p3/2 and 2p1/2, respectively, while 455.85 and 461.89 eV are assigned to 3+ valence state of Ti 2p3/2 and 2p1/2, respectively. Note that these Ti^{4+} and Ti^{3+} peaks in oxygen vacancy rich A500V are due to regular $Ti^{3+}_{lattice}$ and $Ti^{4+}_{lattice}$ in TiO_2 crystals. A comparison of the oxygen O 1s core-level spectra for different Ti_i and O_v rich samples is shown in Figure 3c. Besides the broad shoulder at higher binding energy, intense peaks at 529.17 and 529.23 eV are observed for A900 and B500, respectively. This peak is of lower intensity and at higher biding energy for vacancy rich A500V. XPS peak at 530.1 eV is generally due to the O_2^- ion in TiO_2 crystal lattice.[36,37] Thus, the observed intense O 1s peak in A900 and B500 shifted to lower binding energy by ~0.9 eV

dx.doi.org/10.1021/jp408249q | J. Phys. Chem. C 2013, 117, 23402−23411

may be due to the contribution from Ti_i−O binding on the surface and near surface region.

ESR is an exceptionally powerful technique in detecting the spin polarized charge state of defective TiO_2 nanostructures. ESR spectra shown in Figure 3d reveal that g = 1.972 and 1.942 for B500 and g = 1.970 and 1.944 for B700, indicating the presence of Ti^{3+}at regular lattice position and interstitial position, respectively.[33,38,39] Note that Chester[38] and Kingsbury et al.[39] assigned ESR signal at g = 1.94 to Ti^{3+} interstitial. More recently, Zuo et al.[33] reported the ESR signals at g = 1.975 and 1.944 to Ti^{3+} species which were observed from experimental and simulation studies. These results are in close agreement with our ESR results. The g-value at 1.994, 1.993, and 2.001 are attributed to singly ionized oxygen vacancy F^+ center for B500, B700, and C500, respectively. It is also believed that surface Ti^{3+} would react with adsorbed O_2 which reduced to O^- species and show an ESR signal at g = 2.02.[40] It may be noted that ESR is insensitive to Ti^{4+} species and hence no signal is expected from these species. This observation is very useful to identify the Ti_i^{3+} defects as well oxygen vacancy related $Ti_{lattice}^{3+}$ and F^+ centers.

In Situ Photoluminescence under Controlled Environment. To ascertain the origin of visible and NIR PL emission from TiO_2 nanostructures, we performed in situ PL measurements under controlled environments. The enhancement of visible PL after vacuum annealing strongly supports the fact that the visible PL in the TiO_2 NRb is due to oxygen vacancy induced states. For monitoring the NIR PL under controlled environment, the Ti interstitial rich A900 was mounted inside a high vacuum chamber and the chamber was evacuated to a pressure of 5 × 10^{-5} mbar and PL measurements were performed with 405 nm laser at room temperature (RT) with 10 mW power (at source). Interestingly, the RT PL spectrum under vacuum shows both visible and NIR emission bands (with two peaks at 1.47 and 1.40 eV), as shown in Figure 4a, when excited with 405 nm laser. On the other hand, with the controlled introduction of air (oxygen) in the vacuum chamber, the PL spectrum evolves to a very weak visible emission and a strong NIR emission with a single peak at 1.47 eV. The disappearance of visible emission with air/oxygen exposure is consistent with the fact that oxygen vacancy concentration is dramatically reduced due to the laser induced heating in oxygen environment. This is also accompanied by the disappearance of one of the NIR peak at 1.40 eV. Note that A900 underwent calcinations at 900 °C in air before PL measurement. During PL measurement under vacuum, the laser exposure causes local heating of the sample and introduces oxygen vacancies and some of the lattice Ti^{3+} migrates to the interstitial sites, since the process is equivalent to vacuum annealing. Thus, the strong visible band and the lower energy NIR PL band (at ∼1.40 eV) observed under high vacuum arise from the oxygen vacancy and Ti^{3+} interstitial defects, respectively. The strong NIR PL at ∼1.47 eV remains unchanged in intensity and center position when oxygen is introduced in the vacuum chamber. Thus, the NIR PL originates from a defect that is independent of the oxygen vacancy and Ti^{3+} defects in reduced TiO_2. Our results strongly indicate that Ti^{4+} interstitials that migrate to the surface during the high temperature calcinations are indeed responsible for the NIR PL at 1.47 eV. Thus, the in situ PL under vacuum and oxygen environment enables us to clearly distinguish between defect states caused by Ti^{3+} and Ti^{4+} and O_v defects.

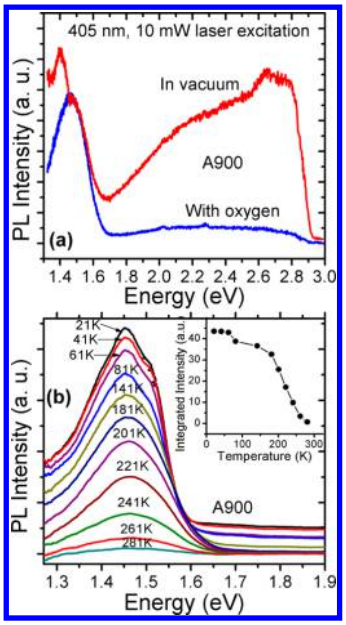

Figure 4. (a) In situ PL spectra for A900 under vacuum and after oxygen exposure with laser ON. The visible emission and lower energy NIR peak drastically goes down, while the other NIR peak at ∼1.47 eV remains unchanged. (b) Low temperature PL spectra under high vacuum for A900 at different temperature. The inset shows change in integrated PL intensity as a function of temperature.

Since laser exposure during PL measurement at room temperature causes dynamic change in defect population in reduced TiO_2 owing to the local heating and oxidation effects, we undertook low temperature PL measurements under high vacuum to ascertain further the origin of NIR PL at ∼1.47 eV. For this experiment, Ti interstitial rich A900 was again chosen that shows strong NIR PL at room temperature and atmospheric pressure (see Figure 2c) and the sample was cooled to a temperature of 11 K under high vacuum. In situ temperature-dependent PL spectra for A900 are shown in Figure 4b. We noticed that at very low temperatures (21−61 K), there is no remarkable change in NIR PL intensity with temperature indicating that laser-induced local heating is not efficient at such low temperatures. Further, the temperature quenching of PL is not significant since PL intensity at low temperature and room temperature was equally high. However, a marked reduction of PL intensity is observed when the sample temperature increased beyond 61 K up to 281 K (see inset of Figure 4b). Note that the intensity of NIR PL at room temperature and atmospheric pressure for A900 was very high prior to the cooling for low temperature PL measurement under high vacuum. Since the measurement was carried out under high vacuum, it may be possible that the oxygen vacancies are increased with the increasing laser heating at higher temperature. If the evolution of NIR PL has any relation to the oxygen vacancy, then the intensity should be enhanced with the increasing temperature. However, because we observed the systematic reduction of NIR PL intensity with increasing sample temperature, the NIR PL cannot be related to oxygen vacancy as well as $Ti_{lattice}^{3+}$ defects. We believe that the gradual decrease of NIR PL by the laser annealing in vacuum is due to the Ti_i migration from the near surface region to the bulk in A900 which occupy the regular Ti lattice site so that there is reduction of Ti_i defects. Note that laser induced local heating is effective when the sample temperature is near room

dx.doi.org/10.1021/jp408249q | J. Phys. Chem. C 2013, 117, 23402−23411

temperature, while for the sample maintained at low temperature the local heating is less efficient due to heat dissipation to the sample holder, despite tight focusing of the laser beam on the sample. Direct evidence for Ti_i migration from surface to bulk of rutile TiO_2 under similar experimental conditions were provided by Henderson[41] through temperature programmed static secondary ion mass spectrometry (SSIMS) measurements. It was demonstrated that when a rutile reduced TiO_2 is vacuum heated above 700 K, the diffusion of Ti interstitial from the surface to bulk takes place, instead of out diffusion of bulk oxygen atoms. More recently, this was demonstrated for anatase TiO_2 as well.[42] Therefore, our results provide clinching evidence that due to the migration of Ti interstitials from surface to the bulk region, the NIR PL at ~1.47 eV gradually diminishes and these surface Ti^{4+} interstitials are unambiguously the origin of the NIR PL at ~1.47 eV in undoped TiO_2 NRb. Note that in the present case Ti interstitial migration may be taking place at a temperature much lower than 700 K, because local heating may not be as high as 700 K with 10 mW (at source) laser excitation. We believe that due to lower sensitivity of the SSIMS that the sensitivity of PL technique, the Ti migration was detected at a higher temperature than the actual temperature required to initiate the process of Ti migration under high vacuum. We anticipate that during laser exposure of the TiO_2 NRb near room temperature, the local temperature rise may be as high as 500 K in TiO_2 nanopowders that may have relatively weak thermal contact with the Si substrate used for the PL measurements and around this temperature Ti_i migration starts taking place that could be monitored through PL due to its extremely high sensitivity. In the case of Si nanocrystal film on quartz substrate, the local temperature rise was found to be as high as ~1000 K for a laser power density of 5 $kWcm^{-2}$ during laser Raman measurements with continuous wave 488 nm laser.[43] Unfortunately, no such data is available for TiO_2 nanostructures. Though the incident laser power density is estimated to be about 1 kW cm^{-2} in our case, accurate estimate of the local temperature rise is not feasible here due to nonavailability of thermal conductivity data for TiO_2 NRb.

In order to gain a better insight into the entire range of bandgap states responsible for the NIR PL peaks, we measured extended NIR PL at room temperature using an InGaAs detector and results are shown in Figure 5a. The NIR peaks are found to be broad and the mean position shows blue-shift as the calcinations temperature is increased. The broad peak consists of two Gaussian peaks centered at 1.27 and 1.47 eV for C500, as shown in Figure 5b. The broad peak may be due to the size distribution of the NRb and broad distribution of electronic sates in the band gap causes bandgap reduction, as observed from absorption studies. As discussed before, these peaks are attributed to Ti^{3+} and Ti^{4+} interstitials. The peak position for Ti^{3+} slightly varies in different samples and the extracted peak positions (peaks P1 and P2) are presented in Table 1. The time-resolved PL (TRPL) studies on C500 at emission energy 1.30 eV show PL decay in microsecond time scale (Figure 5c). The TRPL spectra can be fitted by a biexponential decay curve with time constant τ_1 = 1.1 μS and τ_2 = 32.8 μS. This result reveals that two defect states contribute to the broad NIR PL, consistent with the steady state PL spectrum. The fast decay and slow decay correspond to contributions from peaks at 1.27 eV (P1) and 1.47 eV (P2), respectively. It is observed that peak P2 at 1.47 eV remains unchanged in energy for all samples, while the peak P1 at lower

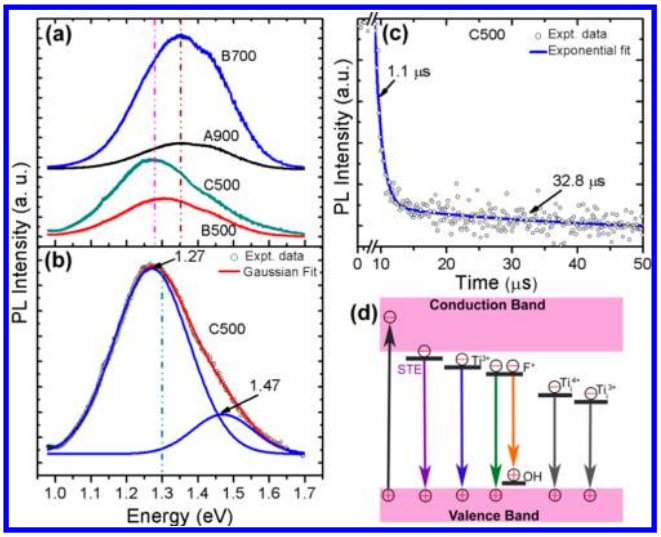

Figure 5. (a) Extended range NIR PL spectra of A900, B500, B700, and C500 using an InGaAs detector. The spectra are vertically shifted for clarity of presentation. Vertical dotted lines indicate the respective peak positions for two groups of samples. (b) Gaussian fit to the NIR PL for C500 showing two symmetric peaks centered at 1.27 and 1.47 eV. (c) TRPL spectrum of C500 at 1.30 eV emission, the symbols represent experimental data and the solid line represents fitted curve with double exponential decay. The time constants of decay are indicated in each case. (d) Schematic band diagram illustrating the physical origin of the visible and NIR PL emissions. See text for details.

energy side varies from 1.21 to 1.34 eV depending upon the samples growth and calcinations temperatures. Hence, the peak P2 at 1.47 eV is attributed to Ti_i^{4+}, while the peak P1 is assigned to Ti_i^{3+} defects. The relative intensities of these two peaks depend on the history of PL measurements environment. Note that XPS results support the presence of both Ti_i^{3+} and Ti_i^{4+} and ESR spectra show the presence of Ti_i^{3+} defects. Therefore, our results are consistent with the fact that the migrated Ti_i^{3+} at the surface interact with O_2 in air during high temperature calcinations and a majority of these species are converted to Ti^{4+} oxidation states. So, the peak P1 is shifted toward higher energy as the calcinations temperature increases. Note that very weak broad NIR PL is also observed for oxygen vacancy rich A500V compared to other as-synthesized samples, with the InGaAs detector, indicating the presence of low concentration of Ti_i defects in A500V. Further we noticed that as the growth temperature increases from 180−235 °C, visible PL band decreases systematically and NIR PL band successively evolves and intensity increases. So, the evolution of NIR PL is dominant at higher temperature heat treatment, that is, both higher growth and calcinations temperatures in air. The samples with strong NIR PL have stronger and extended range visible absorption, as shown in Figure 2. These results strongly suggest that strong visible absorption and NIR PL emission are caused primarily by the Ti interstitial defects. Finally, the effect of various surface morphologies that evolve during calcinations on the visible and NIR PL cannot be fully ignored. Further studies combined with in situ STM and photoelectron spectroscopy may shed more light on the local structure of these defects and distribution of bandgap states in undoped TiO_2 nanostructures.

dx.doi.org/10.1021/jp408249q | J. Phys. Chem. C 2013, 117, 23402−23411

DISCUSSION

Lauer[44] recorded a 1.70 eV NIR PL emission for high temperature annealed (900−1000 °C) ZnO in O_2 ambient and suggested that the PL results from electron transition from the conduction band edge to a hole trapped in the bulk at 1.60 eV above the valence band edge. Recently, Wang et al.[27] reported splitting of broad visible-NIR PL to separate green (2.31 eV) and NIR (1.64 eV) emissions for 800 °C air-annealed ZnO microstructure and finally the NIR band dominated at 1000 °C. They suggested that the NIR emission is due to donor−acceptor transition between oxygen vacancy and zinc vacancy and/or radiative recombination of shallowly trapped electrons with deeply trapped hole at interstitial O_i defect. Shi et al.[22] reported the NIR PL emission at ∼1.49 eV when the TiO_2 was calcined at >500 °C and the peak was more intense after 900 °C calcinations. The authors investigated the in situ PL measurement in O_2 and H_2 treatment as an oxidation and reduction atmosphere for the 900 °C calcined sample and observed that the NIR PL band are increased after oxidation treatment in O_2 and decreased after reduction treatment in H_2. It was suggested that NIR luminescence is due to intrinsic defects in rutile TiO_2. Note that here the B500 is purely anatase, as confirmed from the XRD and Raman analyses. We observed strong NIR PL signal in B500 and A900. Further, we observed the NIR PL emission in pure TiO_2(B), mixed phase TiO_2(B)-anatase and anatase-rutile besides the broad visible PL emission. Our results suggest that NIR PL in TiO_2 is not the intrinsic properties of rutile phase only, contrary to the earlier report.[22] Therefore, it appears that the high temperature heat treatment actually results in the migration of intrinsic defects from the bulk to the surface and evolution of NIR PL emissions in both TiO_2 and ZnO systems.

We noticed that A500, A700, and A900 show the visible PL band intensity in the order A700 > A900 > A500, whereas the NIR PL in the order A900 > A700 > A500. Our experimental results reveal that the calcinations of as-grown solvothermal product at various temperatures in air is a more complex than a simple vacancy filling process as is usually believed, owing to the peculiar behavior of NIR and visible bands observed here. At a typical calcinations temperature, the samples with moderate to high oxygen vacancies and Ti_i defects exhibit a wide variety of restructuring surface morphologies that includes the formation of nanopits, nanobricks and smooth surface on the TiO_2 NRb. These surface structures result from the various $Ti_{lattice}$-O and Ti_i-O bond rearrangements due to the Ti interstitials that diffuse from the bulk to the surface during calcinations. There has been evidence for diffusing native point defects in bulk rutile playing a major role in surface and interface related phenomena when high temperature annealing is involved.[45,46] When a reduced rutile TiO_2 (110) crystal is exposed to O_2 at elevated temperatures, diffusion of Ti interstitial to the surface has been reported[12,47,48] and the opposite effect occurs during vacuum annealing.[13,49] Iddir et al.[50] reported that the Ti interstitials with small migration barriers are the major diffusive species compared to oxygen vacancies by using ab initio calculation. Because the behavior of two PL bands (NIR and visible emission) are different, so it is ascribed to a difference in trapping probability and expected to originate from different sources of point defects in TiO_2 NRb. Therefore, besides the O_v, Ti_i must be also considered as an active defects in reduced TiO_2 and it may strongly influence various properties of the material, such as bandgap narrowing. At moderate calcinations temperature 700 °C, the dehydration of as-grown solvothermal products takes place and the oxygen vacancies are increased for the A700 as compared to A500 and the molecular O_2 may not interact with the material at this stage. At higher temperature 900 °C, the molecular O_2 interacts with surface of the materials and start filling oxygen vacancies and the near surface Ti_i diffuse to the upper surface layer, where reaction with O_2 molecules is more likely. The Ti interstitial diffusion proceeds via an exchange mechanism[50] in which a Ti atom on a regular lattice site is released to an interstitial site toward the surface and subsequently the lattice site is occupied by the original Ti interstitial atom from a deeper layer. So, we believe that the gradual increase of NIR PL with calcinations temperature may be due to the creation of more Ti_i defects in the near surface layers.

Therefore, our experimental finding provide convincing evidence that visible PL primarily originates from oxygen vacancies, while the extended visible absorption as well as NIR PL emission are due to the interstitial Ti_i defects in reduced TiO_2. The native defects such as O_v and Ti_i create deep trap states within the bandgap of TiO_2 which act as luminescence centers for visible and NIR PL, respectively. Note that the Ti_i defect trap states are deeper than the O_v trap states below the conduction band as theoretically predicted by Lee et al.[19] and Finazzi et al.[20] Interestingly, the measured energies for the Ti_i states are close to the theoretically predicted energy levels of 1.3 eV above the valence band[51] or 1.3 eV below the conduction band.[19] Since the measured band gap in the Ti interstitial rich TiO_2 NRb lies in the range 1.98 to 2.64 eV (see Table 1), the predicted results matches remarkably well with our experimental data. The location of these trap states which are responsible for the evolution of strong visible and NIR PL emissions can be understood better from the schematic band diagram shown in Figure 5d. The photogenerated electrons are initially excited to the conduction band of TiO_2 on irradiating laser light (405 nm) and then relaxed to the defect states. The visible PL is due to the transition of electrons from self-trap exciton, Ti_i^{3+} center and F^+ center trap states to the valence band and F^+ center state to acceptor level due to OH^- species, as discussed in our earlier report.[24] The NIR PL emissions are due to the transition of electron from Ti_i^{4+} and Ti_i^{3+} defect trap states to the valence band.

CONCLUSIONS

Undoped TiO_2 NRb with nanopits, nanobricks, and nanostones like surface morphologies were successfully synthesized by a simple solvothermal method followed by calcinations. With higher calcination temperatures, absorption edge systematically red-shift up to visible (yellow-red) region for these undoped NRb, which is very important for enhanced visible light photocatalysis. Our in situ PL studies under controlled environment provide conclusive evidence that visible PL band originate from oxygen vacancy states that can be manipulated easily. Low temperature in situ PL studies provide clinching evidence for the Ti surface interstitials being responsible for the NIR PL emission at 1.27 and 1.47 eV, identified for the first time. The UV-visible-NIR absorption spectroscopy shows reduced bandgap due to the presence of O_v and Ti_i defect states within the band gap of TiO_2 NRb. Furthermore, the XPS and ESR studies confirmed the presence of O_v and Ti_i defects in the NRb in different samples, depending upon different growth conditions and post growth processing. The highly porous TiO_2 NRb developed in this work accompanied by

dx.doi.org/10.1021/jp408249q | J. Phys. Chem. C 2013, 117, 23402−23411

identification of the defects responsible for strong visible absorption and NIR PL emission is considered as an important milestone for engineering the efficient visible light photocatalytic and photovoltaic applications of undoped TiO_2-based materials.

■ ASSOCIATED CONTENT

Supporting Information

Details of the characterization techniques, additional FESEM images, EDX spectrum, XRD patterns, Raman spectra, and UV−visible absorption spectrum of precursor TiO_2 nanoparticles are presented. This material is available free of charge via the Internet at http://pubs.acs.org.

■ AUTHOR INFORMATION

Corresponding Author

*E-mail: giri@iitg.ernet.in.

Notes

The authors declare no competing financial interest.

■ REFERENCES

(1) Wang, G.; Wang, H.; Ling, Y.; Tang, Y.; Yang, X.; Fitzmorris, R. C.; Wang, C.; Zhang, J. Z.; Li, Y. Hydrogen-Treated TiO_2 Nanowire Arrays for Photoelectrochemical Water Splitting. *Nano Lett.* **2011**, *11*, 3026−3033.

(2) Chen, X.; Liu, L.; Yu, P. Y.; Mao, S. S. Increasing Solar Absorption for Photocatalysis with Black Hydrogenated Titanium Dioxide Nanocrystals. *Science* **2011**, *331*, 746−750.

(3) Zhang, Y.; Fu, W.; Yang, H.; Qi, Q.; Zeng, Y.; Zhang, T.; Ge, R.; Zou, G. Synthesis and Characterization of TiO_2 Nanotubes for Humidity Sensing. *Appl. Surf. Sci.* **2008**, *254*, 5545−5547.

(4) Zukalova, M.; Kalbac, M.; Kavan, L.; Exnar, I.; Graetzel, M. Pseudocapacitive Lithium Storage in TiO_2(B). *Chem. Mater.* **2005**, *17*, 1248−1255.

(5) Xu, C.; Shin, P. H.; Cao, L.; Wu, J.; Gao, D. Ordered TiO_2 Nanotube Arrays on Transparent Conductive Oxide for Dye-Sensitized Solar Cells. *Chem. Mater.* **2010**, *22*, 143−148.

(6) Wolf, S. A.; Awschalom, D. D.; Buhrman, R. A.; Daughton, J. M.; Von Molnar, S.; Roukes, M. L.; Chtchelkanova, A. Y.; Treger, D. M. Spintronics: A Spin-Based Electronics Vision for the Future. *Science* **2001**, *294*, 1488−1495.

(7) Kuznetsov, V. N.; Serpone, N. On the Origin of the Spectral Bands in the Visible Absorption Spectra of Visible-Light-Active TiO_2 Specimens Analysis and Assignments. *J. Phys. Chem. C* **2009**, *113*, 15110−15123.

(8) Naldoni, A.; Allieta, M.; Santangelo, S.; Marelli, M.; Fabbri, F.; Cappelli, S.; Bianchi, C. L.; Psaro, R.; Santo, V. D. Effect of Nature and Location of Defects on Bandgap Narrowing in Black TiO_2 Nanoparticles. *J. Am. Chem. Soc.* **2012**, *134*, 7600−7603.

(9) Liu, X.; Gao, S.; Xu, H.; Lou, Z.; Wang, W.; Huang, B.; Dai, Y. Green Synthetic Approach for Ti^{3+} Self-Doped TiO_{2-x} Nanoparticles with Efficient Visible Light Photocatalytic Activity. *Nanoscale* **2013**, *5*, 1870−1875.

(10) Chen, X.; Burda, C. The Electronic Origin of the Visible-Light Absorption Properties of C-, N-, and S-Doped TiO_2 Nanomaterials. *J. Am. Chem. Soc.* **2008**, *130*, 5018−5019.

(11) Chen, X.; Liu, L.; Liu, Z.; Marcus, M. A.; Wang, W.-C.; Oyler, N. A.; Grass, M E.; Mao, B.; Glans, P.; Yu, P. Y.; et al. Properties of Disorder-Engineered Black Titanium Dioxide Nanoparticles through Hydrogenation. *Sci. Rep.* **2013**, *3*, 1510.

(12) Wendt, S.; Sprunger, P. T.; Lira, E.; Madsen, G. K. H.; Li, Z.; Hansen, J. Ø.; Matthiesen, J.; Rasmussen, A. B.; Lægsgaard, E.; Hammer, B.; et al. The Role of Interstitial Sites in the Ti 3*d* Defect State in the Band Gap of Titania. *Science* **2008**, *320*, 1755−1759.

(13) Henderson, M. A. A Surface Perspective on Self-Diffusion in Rutile TiO_2. *Surf. Sci.* **1999**, *419*, 174−187.

(14) Hoffmann, M. R.; Martin, S. T.; Choi, W.; Bahnemann, D. W. Environmental Applications of Semiconductor Photocatalysis. *Chem. Rev.* **1995**, *95*, 69−96.

(15) Choi, W.; Termin, A.; Hoffmann, M. R. Einflüsse Von Dotierungs-Metall-Ionen auf Die Photokatalytische Reaktivität Von TiO_2-Quantenteilchen. *Angew. Chem.* **1994**, *106*, 1148−1149.

(16) Asahi, R.; Morikawa, T.; Ohwaki, T.; Aoki, K.; Taga, Y. Visible-Light Photocatalysis in Nitrogen-Doped Titanium Oxides. *Science* **2001**, *293*, 269−271.

(17) Choi, W.; Termin, A.; Hoffmann, M. R. The Role of Metal Ion Dopants in Quantum-Sized TiO_2: Correlation between Photoreactivity and Charge Carrier Recombination Dynamics. *J. Phys. Chem.* **1994**, *98*, 13669−13679.

(18) Tao, J.; Luttrell, T.; Batzill, M. A Two-Dimensional Phase of TiO_2 with a Reduced Bandgap. *Nat. Chem.* **2011**, *3*, 296−300.

(19) Lee, H. −Y.; Clark, S. J.; Roberton, J. Calculation of Point Defects in Rutile TiO_2 by the Screened-Exchange Hybrid Functional. *Phys. Rev. B* **2012**, *86*, 075209.

(20) Finnazzi, E.; Valentin, C. D.; Pachhioni, G. Nature of Ti Interstitials in Reduced Bulk Anatase and Rutile TiO_2. *J. Phys. Chem. C* **2009**, *113*, 3382−3385.

(21) Henderson, M. A.; Epling, W. S.; Peden, C. H. F.; Perkins, C. L. Insights into Photoexcited Electron Scavenging Processes on TiO_2 Obtained from Studies of the Reaction of O_2 with OH Groups Adsorbed at Electronic Defects on TiO_2(110). *J. Phys. Chem. B* **2003**, *107*, 534−545.

(22) Shi, J.; Chen, J.; Feng, Z.; Chen, T.; Lian, Y.; Wang, X.; Li, C. Photoluminescence Characteristics of TiO_2 and Their Relationship to the Photoassisted Reaction of Water/Methanol Mixture. *J. Phys. Chem. C* **2007**, *111*, 693−699.

(23) Yang, M.; Liu, W.; Sun, J. −L.; Zhu, J. −L. High Magnetic Field Annealing Effect on Visible Photoluminescence Enhancement of TiO_2 Nanotube Arrays. *Appl. Phys. Lett.* **2012**, *100*, 043106.

(24) Santara, B.; Giri, P. K.; Imakita, K.; Fujii, M. Evidence of Oxygen Vacancy Induced Room Temperature Ferromagnetism in Solvothermally Synthesized Undoped TiO_2 Nanoribbons. *Nanoscale* **2013**, *5*, 5476−5488.

(25) Wang, X.; Feng, Z.; Shi, J.; Jia, G.; Shen, S.; Zhou, J.; Li, C. Trap States and Carrier Dynamics of TiO_2 Studied by Photoluminescence Spectroscopy Under Weak Excitation Condition. *Phys. Chem. Chem. Phys.* **2010**, *12*, 7083−7090.

(26) Montoncello, F.; Carotta, M. C.; Cavicchi, B.; Ferroni, M.; Giberti, A.; Guidi, V.; Malagu, C.; Martinelli, G.; Meinardi, F. Near-Infrared Photoluminescence in Titania: Evidence for Phonon-Replica Effect. *J. Appl. Phys.* **2003**, *94*, 1501−1505.

(27) Wang, M.; Zhou, Y.; Zhang, Y.; Kim, E. J.; Hahn, S. H.; Seong, S. G. Near-Infrared Photoluminescence from ZnO. *Appl. Phys. Lett.* **2012**, *100*, 101906.

(28) Parker, J. C.; Seigel, R. W. Calibration of the Raman Spectrum to the Oxygen Stoichiometry of Nanophase TiO_2. *Appl. Phys. Lett.* **1990**, *57*, 943−945.

(29) Zhang, W. F.; He, Y. L.; Zhang, M. S.; Yin, Z.; Chen, Q. Raman Scattering Study on Anatase TiO_2 Nanocrystals. *J. Phys. D: Appl. Phys.* **2000**, *33*, 912−916.

(30) Santara, B.; Pal, B.; Giri, P. K. Signature of Strong Ferromagnetism and Optical Properties of Co Doped TiO_2 Nanoparticles. *J. Appl. Phys.* **2011**, *110*, 114322.

(31) Morgan, B. J.; Watson, G. W. Intrinsic *n*-Type Defect Formation in TiO_2: A Comparison of Rutile and Anatase from GGA+*U* Calculations. *J. Phys. Chem. C* **2010**, *114*, 2321−2328.

(32) Justicia, I.; Ordejon, P.; Canto, G.; Mozos, J. L.; Fraxedes, J.; Battiston, G. A.; Gerbasi, R.; Figueras, A. Designed Self-Doped Titanium Oxide Thin Films for Efficient Visible-Light Photocatalysis. *Adv. Mater.* **2002**, *14*, 1399−1402.

(33) Zuo, F.; Wang, L.; Wu, T.; Zhang, Z.; Borchardt, D.; Feng, P. Self-Doped Ti^{3+} Enhanced Photocatalyst for Hydrogen Production under Visible Light. *J. Am. Chem. Soc.* **2010**, *132*, 11856−11857.

(34) Wang, J.; Wang, Z.; Huang, B.; Ma, Y.; Liu, Y.; Qin, X.; Zhang, X.; Dai, Y. Oxygen Vacancy Induced Band-Gap Narrowing and

Enhanced Visible Light Photocatalytic Activity of ZnO. *ACS Appl. Mater. Interfaces* **2012**, *4*, 4024−4030.
(35) Etacheri, V.; Seery, M. K.; Hinder, S. J.; Pillai, S. C. Oxygen Rich Titania: A Dopant Free, High Temperature Stable, and Visible-Light Active Anatase Photocatalyst. *Adv. Funct. Mater.* **2011**, *21*, 3744−3752.
(36) Cao, C.; Hu, C.; Shen, W.; Wang, S.; Wang, J.; Tian, Y. Fabrication of a Novel Heterostructure of Co_3O_4-Modified TiO_2 Nanorod Arrays and Its Enhanced Photoelectrochemical Property. *J. Alloys Compd.* **2013**, *550*, 137−143.
(37) Abazović, N. D.; Mirenghi, L.; Janković, I. A.; Bibić, N.; Šojić, D. V.; Abramović, B. F.; Čomor, M. I. Synthesis and Characterization of Rutile TiO_2Nanopowders Doped with Iron Ions. *Nanoscale Res. Lett.* **2009**, *4*, 518−525.
(38) Chester, C. F. Electron Spin Resonance in Semiconducting Rutile. *J. Appl. Phys.* **1961**, *32*, 2233−2236.
(39) Kingsburg, P. I., Jr.; Ohlsen, W. D.; Johnson, O. W. Defects in Rutile. I. Electron Paramagnetic Resonance of Interstitially Doped *n*-Type Rutile. *Phys. Rev. B* **1968**, *175*, 1091−1098.
(40) Anpo, M.; Che, M.; Fubini, B.; Garrone, E.; Giamello, E.; Paganini, M. C. Generation of Superoxide Ions at Oxide Surfaces. *Top. Catal.* **1999**, *8*, 189−198.
(41) Henderson, M. A. Mechanism for the Bulk-Assisted Reoxidation of Ion sputtered TiO_2 Surfaces: Diffusion of Oxygen to the Surface or Titanium to the Bulk? *Surf. Sci.* **1995**, *343*, L1156−L1160.
(42) Herman, G. S.; Zehr, R. T.; Henderson, M. A. Characterization of Oxygen and Titanium Diffusion at the Anatase $TiO_2(001)$ Surface. *Surf. Sci.* **2013**, *612*, L5−L8.
(43) Mavi, H. S.; Prusty, S.; Shukla, A. K.; Abbi, S. C. Continuous Wave Laser-Induced Temperature Rise in the Thin Films of Silicon Nanocrystals Using Raman Scattering. *Thin Solid Film* **2003**, *425*, 90−96.
(44) Lauer, R. B. The IR Photoluminescence Emission Band in ZnO. *J. Phys. Chem. Solids* **1973**, *34*, 249−253.
(45) Diebold, U. The Surface Science of Titaniun Dioxide. *Surf. Sci. Rep.* **2003**, *48*, 53−229.
(46) Dulub, O.; Hebenstreit, W.; Diebold, U. Imaging Cluster Surfaces with Atomic Resolution: The Strong Metal-Support Interaction State of Pt Supported on $TiO_2(110)$. *Phys. Rev. Lett.* **2000**, *84*, 3646−3649.
(47) Onishi, H.; Iwasawa, Y. Dynamic Visualization of a Metal-Oxide-Surface/Gas-Phase Time-Resolved Observation by Scanning Tunneling Microscopy at Reaction: 800 K. *Phys. Rev. Lett.* **1996**, *76*, 791−794.
(48) Bennett, R. A.; Stone, P.; Price, N. J.; Bowker, M. Two (1×2) Reconstructions of $TiO_2(110)$: Surface Rearrangement and Reactivity Studied Using Elevated Temperature Scanning Tunneling Microscopy. *Phys. Rev. Lett.* **1999**, *82*, 3831−3834.
(49) Park, K. T.; Pan, M.; Meunier, V.; Plumer, E. W. Reoxidation of $TiO_2(110)$ via Ti Interstitials and Line Defects. *Phys. Rev. B* **2007**, *75*, 245415.
(50) Iddir, H.; Oğut, S.; Zapol, P.; Browning, N. D. Diffusion Mechanisms of Native Point Defects in Rutile TiO_2: Ab Initio Total-Energy Calculations. *Phys. Rev. B* **2007**, *75*, 073203.
(51) Nolan, M.; Elliott, S. D.; Mulley, J. S.; Bennett, R. A.; Basham, M.; Mulheran, P. Electronic Structure of Point Defects in Controlled Self-Doping of The TiO_2 (110) Surface: Combined Photoemission Spectroscopy and Density Functional Theory Study. *Phys. Rev. B* **2008**, *77*, 235424.